Physics of Plasmas

LETTER | MAY 01 2024

On the role of target mass in extreme ultraviolet light generation from CO_2-driven tin plasmas for nanolithography

Special Collection: Plasma Sources for Advanced Semiconductor Applications

J. Gonzalez ; J. Sheil

Phys. Plasmas 31, 050701 (2024)
https://doi.org/10.1063/5.0200206

On the role of target mass in extreme ultraviolet light generation from CO_2-driven tin plasmas for nanolithography

Cite as: Phys. Plasmas **31**, 050701 (2024); doi: 10.1063/5.0200206
Submitted: 25 January 2024 · Accepted: 12 April 2024 ·
Published Online: 1 May 2024

J. Gonzalez[1] and J. Sheil[1,2,a)]

AFFILIATIONS

[1]Advanced Research Center for Nanolithography, Science Park 106, 1098 XG Amsterdam, The Netherlands
[2]Department of Physics and Astronomy, and LaserLaB, Vrije Universiteit Amsterdam, De Boelelaan 1081, 1081 HV Amsterdam, The Netherlands

Note: This paper is part of the Special Topic: Plasma Sources for Advanced Semiconductor Applications.
[a)]**Author to whom correspondence should be addressed:** j.sheil@arcnl.nl

ABSTRACT

Target conditioning is a crucial ingredient of high-power extreme ultraviolet (EUV) source operation in state-of-the-art nanolithography. It involves deforming tin microdroplets into tens of nanometer-thin sheets, sheets which are subsequently irradiated by intense CO_2 laser radiation to form a hot, EUV-emitting plasma. Recent experiments have found that a substantial fraction of the initial droplet mass is lost in the deformation phase through fragmentation. The goal of the present study is to investigate, using radiation-hydrodynamic modeling, how variations in the sheet mass affect EUV source power and the laser-to-in-band conversion efficiency (CE). It is found that high-mass sheets can "feed" the plasma with sufficient mass to sustain the production of in-band-emitting charge states over the course of laser irradiation. Low-mass sheets, on the contrary, cannot supply enough mass to sustain this production over the pulse, thus leading to a reduction in in-band power and CE. The dependence of CE on laser energy and target thickness is quantified, and a rather weak reduction of CE with increasing laser energy for high-mass sheets is identified.

State-of-the-art extreme ultraviolet (EUV) light production for nanolithography is based on irradiating tin targets with CO_2 laser radiation to form an intense, EUV-emitting plasma.[1–3] The source of this radiation is largely atomic transitions in multiple charged tin ions of charge $Z \in [11, 15]$.[4–6] Of prime interest to the industry is EUV radiation contained in a narrow 2% bandwidth centered at 13.5 nm (Refs. 4, 5, 7, and 8) (the "in-band" region) as this radiation can be transported and shaped for the lithographic process using Mo/Si multilayer mirrors.[9] These plasmas are formed on thin sheet-like targets achieved by deforming tin microdroplets through pre-pulse laser irradiation.[10–14] This process, known as target conditioning, is crucial for achieving high conversion efficiencies (CE—ratio of in-band energy radiated toward the plasma-facing collector mirror to laser energy) from plasmas driven by the aforementioned CO_2 main pulse laser.[2,15,16]

In recent target-conditioning studies, Liu *et al.*[17–19] found that a high fraction of the initial droplet mass, between one-half to three-quarters, is lost during the deformation phase through fragmentation. This has important implications for target optimization; if one wants to maximize the amount of tin mass available for EUV production, one must either (i) reduce the time between pre- and main-pulse irradiation[19] and/or (ii) increase the pre-pulse intensity to expedite sheet formation.[17] The formed sheets typically have radii between 200 and 300 μm and thicknesses between 20 and 50 nm. A lossless, i.e., "fragment-less," deformation of a $D = 30$ μm diameter droplet[2] into a disk of the same radius would, however, result in a thickness of $\sim$100 nm. It is an open question how variations in the total sheet mass affect EUV source performance, e.g., in-band power and CE. It is the goal of the current study to investigate this dependency.

Early radiation-hydrodynamic modeling efforts of Nishihara *et al.*,[16] as well as the more recent work of Sunahara *et al.*,[20] have found that CO_2 laser irradiation of a pre-formed plasma can increase CO_2 laser absorption and, consequentially, the CE. However, as noted by Sunahara *et al.*,[20] little is known about the pre-formed plasma density profile from a quantitative perspective.[20] In fact, only quite recently have detailed measurements of the electron density and temperature in

hot, CO_2-driven plasmas been performed,[21,22] and extension of these measurements to the pre-formed plasma regime would provide important information for model benchmarking. A previous study by Basko[23] explored the use of a "slave" laser to form a pre-plasma from a droplet target which, after main pulse irradiation, resulted in CEs of 8%–9%. To circumvent uncertainties in the pre-formed plasma density profile, we do not consider a pre-plasma in the present work. Rather, we focus solely on CO_2 laser irradiation of thin tin sheets to unequivocally determine the role of the sheet mass on EUV source performance. Specifically, we have simulated CO_2 laser irradiation of tin sheets of radius $R = 200\,\mu$m of differing initial thickness and density: targets having initial thickness $t_s = 100$, 50, and 33 nm and constant density $\rho = 6.9\,\mathrm{g\,cm^{-3}}$ are compared to targets having initial density $\rho = 5.0$, 3.0, and $2.0\,\mathrm{g\,cm^{-3}}$ and fixed initial thickness $t_s = 100$ nm. The target is, therefore, a perfect disk of constant thickness, with a sheet mass $m_s = \rho\pi R^2 t_s$. The independent sweeps of target thickness and density clarify whether changes in the radiative properties of the plasma are solely dependent on the sheet mass. Consideration of other target features, such as the central mass or bounding rim,[17,19] is postponed to a future study.

We have performed two-dimensional radiation-hydrodynamic simulations using the RALEF-2D[24–26] code, which has found extensive application in EUV source modeling in recent times.[23,27–29] The code solves the equations of single-fluid, single-temperature hydrodynamics accounting for energy transfer processes of thermal conduction, laser transport, and thermal radiation transport. The equation of quasi-static radiation transfer is solved in the local thermodynamic equilibrium approximation using absorption coefficients derived from the THERMOS code.[30,31] The equation-of-state (EOS) of tin is built using the Frankfurt EOS model.[32–34] We have adopted a hybrid model of laser transport that couples a geometrical optics ray-tracing approach with a wave-optics treatment in the underdense plasma.[35] The temporal profile of the laser pulse, depicted by the gray line in Fig. 1 (arbitrary units), follows a typical CO_2 pulse[36–38] with a peak intensity at $t \sim 7$ ns. The employed spatial profile is an ideal flat-top[39] enclosing $\pm 175\,\mu$m, depicted as a shadowed region in the top left frame of Fig. 4. We define an average intensity $\tilde{I}_{las}$, equivalent to full-width-at-half-maximum definition typically used for Gaussian temporal profiles, by dividing the laser energy by the laser spot size (πR_{las}^2 where $R_{las} = 175\,\mu$m) and by the time at which the laser pulse reaches 76% of the total energy ($t = 31$ ns). To clarify the role of sheet mass on EUV production, we employ a single pulse energy of 400 mJ ($\tilde{I}_{las} \simeq 1.34 \times 10^{10}\,\mathrm{W cm^{-2}}$) (close to that which maximizes the CE) in the simulations. Following this, we scan the laser energy over the range $100 - 800$ mJ ($0.34 - 2.68 \times 10^{10}\,\mathrm{W cm^{-2}}$) to investigate the dependence of CE on both laser energy and target thickness.

In Fig. 1(a), we present the temporal evolution of the in-band power radiated into the collector mirror-subtending 2π solid angle, P_{inb}, for targets of varying initial thickness with fixed density (solid lines) and targets of differing initial density with fixed thickness (dashed lines). The variable-density cases are chosen such that the total mass in the sheet is similar to the equivalent variable-thickness case. Examining Fig. 1(a), we see that all targets exhibit a similar in-band power profile up to $t \sim 25$ ns, with a shape similar to that of the CO_2 laser profile shown in gray. Beyond 25 ns, only the two cases with the highest m_s ($t_s = 100$ nm and $\rho = 6.9$, $5.0\,\mathrm{g\,cm^{-3}}$) sustain moderate in-band powers over the entire pulse. Reducing the target mass leads

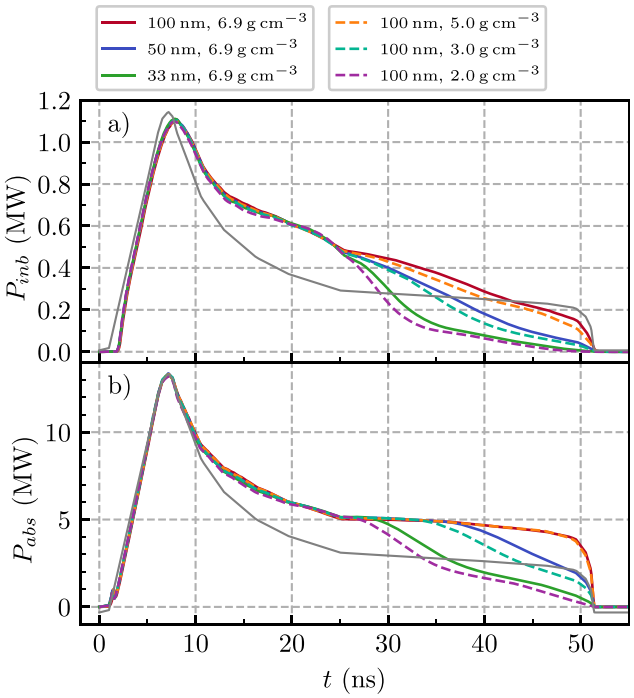

FIG. 1. (a) In-band power P_{inb} in MW radiated into the collector mirror-subtending 2π solid angle and (b) absorbed power for the cases studied in this work. Solid lines correspond to the thickness sweep and dashed lines represent the density sweep. The laser temporal profile in arbitrary units is shown by the gray solid line in both subplots. A laser energy of 400 mJ was employed in the simulations.

to a quenching of in-band powers at earlier times in the pulse. It is also important to note the strong similarity in power profiles for cases of similar m_s. It is interesting to note that the absorbed power, depicted in Fig. 1(b), does not follow the same trend as the in-band power, but, as expected, reduces with decreasing target mass.

To explain the time evolution of in-band power presented in Fig. 1(a), we show in Fig. 2 the evolution of the total mass $m_{\bar{Z}}$ associated with an average charge state $\bar{Z} \in [\bar{Z}_1, \bar{Z}_2)$ at each instant of time for the cases where the target thickness is varied. Recall from above that atomic transitions in charge states $\bar{Z} \in [11, 15]$ are responsible for intense in-band radiation emanating from such plasmas, and, thus, the temporal evolution of their populations underlies the in-band power profiles shown in Fig. 1(a). While the distribution of charge states up to $t \sim 15$ ns is similar for all cases, substantial differences emerge at later times. The $t_s = 100$ nm case shown in Fig. 2(a) exhibits a rather gradual transition from high charge states ($\bar{Z} \in [14, 15)$) to low charge states ($\bar{Z} \in [9, 10)$) over the course of the laser pulse. Reducing the sheet mass by reducing the target thickness [Figs. 2(b) and 2(c)] has the effect of increasing the rate at which the average charge state is quenched. This is most evident for average charge states in the range $\bar{Z} \in [11, 12)$ (green), $[10, 11)$ (blue), and $[9, 10)$ (red). The quenching of charge states below $\bar{Z} \in [10, 11)$ is the cause of the reduction of in-band power after $t \sim 25$ ns observed in Fig. 1(a). In essence, high-mass sheets can "feed" the plasma with sufficient mass to sustain the production of in-band-emitting charge states over the majority of the pulse. Low-mass sheets, on the contrary, cannot supply enough mass

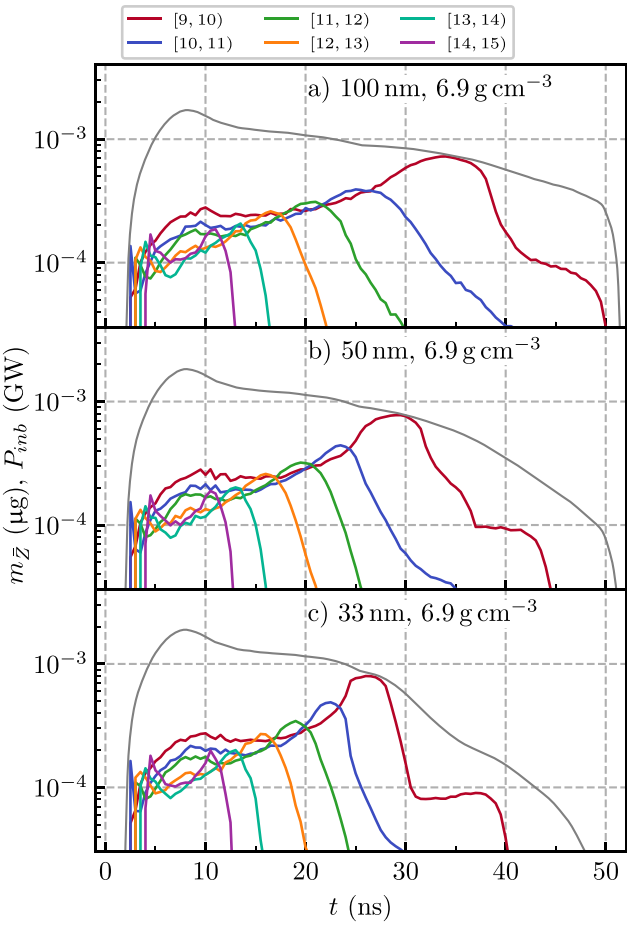

FIG. 2. Total mass $m_{\bar{Z}}$ associated with an average charge state $\bar{Z} \in [\bar{Z}_1, \bar{Z}_2)$ for targets of thickness (a) 100, (b) 50, and (c) 33 nm as a function of time. The gray solid lines represent the in-band powers shown in Fig. 1(a). A laser energy of 400 mJ was employed in the simulations.

over the entire pulse to sustain high in-band powers. The thickness-independent flattening of the $\bar{Z} \in [9, 10)$ curve (shown in red) at late times arises from the formation of a small plasma volume [akin to that shown in Fig. 4(c) for $t = 32$ ns] that persists over an extended time. At this time, laser absorption is low and the plasma average charge state remains relatively constant until sudden extinction.

We now consider the conversion efficiency associated with this irradiation scheme. Suppose that the studied sheets are formed from laser irradiation of a $D = 30\,\mu$m-diameter droplet having a mass $m_d = \frac{4}{3}\pi(\frac{D}{2})^3$ (similar to that used in industrial EUV sources[2]) In Fig. 3, we plot the CE as a function of the ratio m_s/m_d, which indicates a noteworthy reduction of CE with decreasing m_s. This is attributed to the strong collapse of in-band power midway through the pulse, as is observed in Fig. 1(a). From this figure, we also see that the trend of CE is the same irrespective of reducing the target thickness (hollow symbols) or the target density (filled symbols). It is, therefore, the target mass m_s that ultimately determines the achievable CE in this irradiation scheme.

It is important to acknowledge that the CE values reported here are associated with a rather idealized irradiation scheme: a perfect

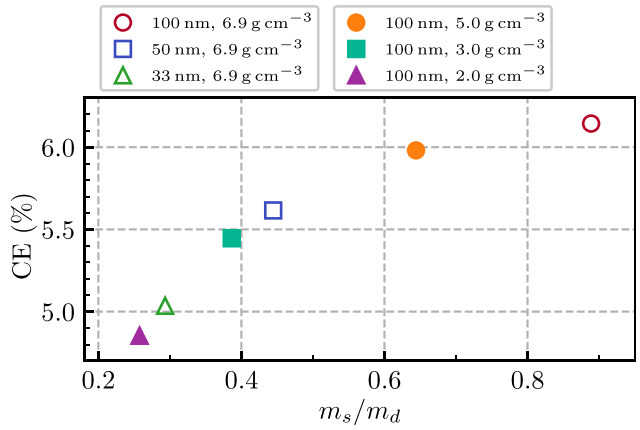

FIG. 3. Dependence of CE on the ratio of sheet mass m_s to droplet mass m_d. Hollow symbols correspond to the thickness sweep, and filled symbols correspond to the density sweep. A laser energy of 400 mJ was employed in the simulations.

flat-top laser profile, a noiseless temporal profile, as well as a uniform target structure without a rim or center mass feature.[17–19] The difference between our CE predictions and the experimental value CE $\sim 3.7\%$ reported in Ref. 2 may be attributed to differences in the structures of the disk targets and/or the laser profiles. The CE metric is also very sensitive to the radiative data (opacities, emissivities) employed in a rad-hydro code (see Ref. 40 for a recent review of a code comparison activity on this topic), and experimental benchmarking is, thus, crucial for the development of predictive modeling capabilities. The key takeaway from Fig. 3 is, therefore, not the exact value of CE predicted by the simulations, but rather the significant reduction in CE when moving from high- to low-mass sheets.

The spatial distribution of plasma properties is also affected by variations in m_s. In Fig. 4 (multimedia view), we present the spatial distribution of the average charge state $\bar{Z}$ (shown in the z-r plane for $r > 0$) and the net balance of produced minus absorbed in-band power (positive shown in purple, negative shown in orange) per unit volume p_{inb} (Ref. 29) (shown in the z-r plane for $r < 0$) for initial target thicknesses of (a) 100, (b) 50, and (c) 33 nm at times $t = 10$ (upper panel) and 32 ns (lower panel) after laser pulse initiation. From the analysis above, we know that the CE of the current irradiation scheme depends solely on m_s, and, thus, it suffices to study cases of varying initial thickness at constant density. At $t = 10$ ns, the spatial distribution of the plasma on the laser-irradiated side is similar for all thickness cases, which explains the overlap of the various P_{inb} curves shown in Fig. 1(a). That said, we also see clear differences in the net absorption of in-band radiation by the target (dark orange region near $z = 0$ mm). By $t = 32$ ns, however, the spatial plasma profiles acquire vastly different shapes depending on the initial target mass. The conical shape of the critical electron surface (red curve) arises due to disparate axial and radial velocities, i.e., the axial velocity is homogeneous due to the spatial flat-top profile while the radial velocity increases toward the edge of the laser profile, $r = 175\,\mu$m. A significant contraction of the critical electron density surface is seen for low-mass targets, resulting in a reduction in laser absorptivity (laser light simply passes above/below the target) and a subsequent drop in P_{inb}.

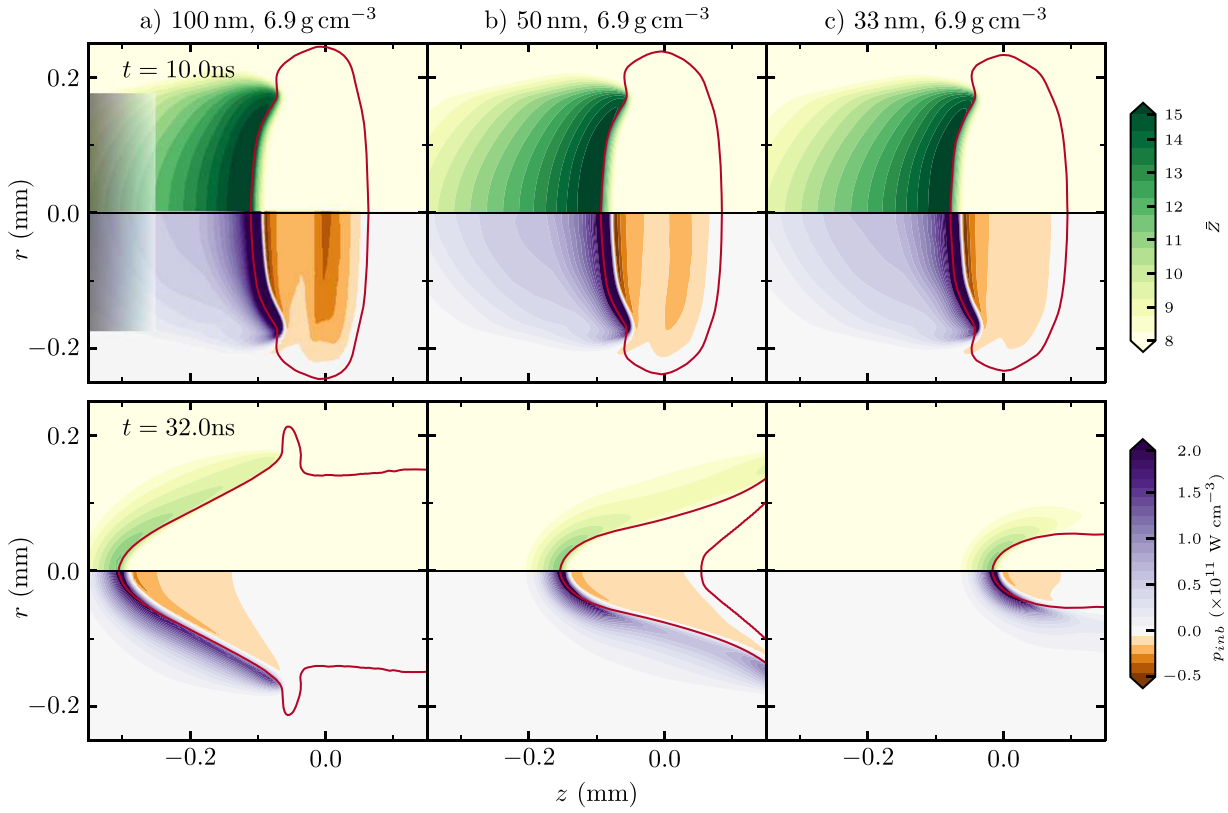

FIG. 4. Spatial distribution of average charge state $\bar{Z}$ (z-r plane for $r > 0$) and the net balance of produced minus absorbed in-band power (positive shown in purple and negative shown in orange) per unit volume p_{inb} (z-r plane for $r < 0$) for target thicknesses of (a) 100, (b) 50, and (c) 33 nm at times $t = 10$ (upper row) and 32 ns (lower row) after pulse initiation. A laser energy of 400 mJ was employed in the simulations. The red solid line represents the critical electron density of CO_2 laser light, $n_e = 10^{19}$ cm^{-3}. The shadowed area in the top left frame depicts the laser beam. Multimedia available online.

Finally, we investigate the dependence of CE on laser energy and target thickness, the results of which are shown in Fig. 5. The simulations employed target thicknesses of 100 nm (red circles), 50 nm (blue squares), and 33 nm (green triangles) with fixed initial density $\rho = 6.9\,\mathrm{g\,cm^{-3}}$, and the solid lines simply serve to connect data points. A sharp rise in CE with increasing laser energy is found for all thickness cases. Moreover, the laser energy that maximizes CE increases with increasing target thickness, i.e., m_s. Considering the highest m_s case (red circles), increasing the laser energy beyond the CE-maximal yields only a minor reduction in CE (a similar observation was made in Ref. 29 for Nd:YAG illumination of tin microdroplets). A stronger reduction in CE with increasing laser energy is identified for the lower mass targets ($\sim$0.7% and $\sim$1%, respectively). Again, it is the sheet mass m_s that plays the defining role here.

To understand the thickness-dependent reduction in CE from the optimal value at 400 mJ, we plot in Fig. 6 the temporal variation of the mass associated with the average charge states $\bar{Z} \in [9, 10)$ and $\bar{Z} \in [14, 15)$ for 800 mJ irradiation. The case with a higher target mass (solid lines) sustains the EUV-emitting plasma for longer compared to the 400 mJ case [Fig. 2(a)], while the extinction of the low-mass target (dotted lines) happens at a similar time ($\sim$30 ns) as the 400 mJ case

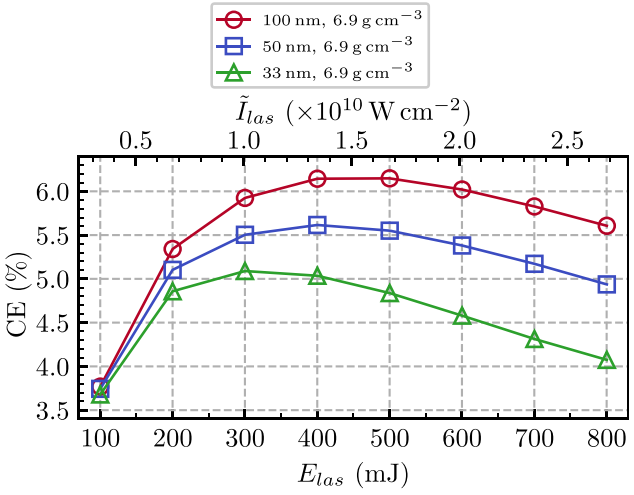

FIG. 5. CE as a function of laser energy for the target thicknesses of (a) 100 (red circles), (b) 50 (blue squares), and (c) 33 nm (green triangles). Equivalent intensity $\tilde{I}_{las}$ shown as a secondary horizontal axis for reference.

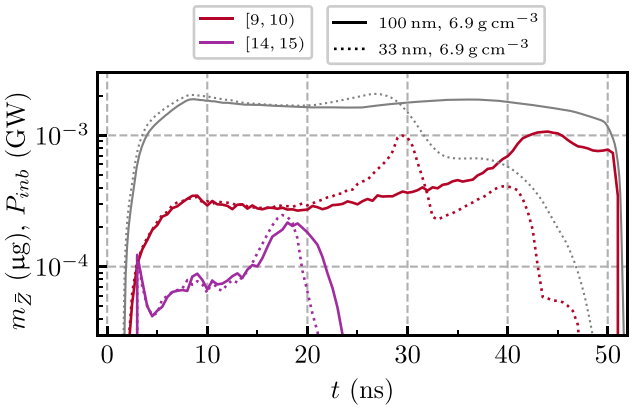

FIG. 6. Total mass $m_{\bar{Z}}$ associated with an average charge state $\bar{Z} \in [9, 10)$ and $\bar{Z} \in [14, 15)$ for targets of thickness 100 (solid line) and 33 nm (dotted line) as a function of time. A laser energy of 800 mJ was employed. The gray lines represent the in-band power for each thickness.

[Fig. 2(c)]. This evolution underlies the in-band power profiles (solid and dotted gray lines), which, for equal input laser energy, results in the stronger CE reduction for the low-mass target (Fig. 5).

In conclusion, we have investigated the role of sheet mass on EUV production in CO_2-driven tin plasmas for nanolithography. We have found that high-mass sheets can supply the plasma with sufficient mass to sustain the production of in-band-emitting charge states over the majority of laser pulse irradiation. Low-mass sheets, on the contrary, cannot supply enough mass to sustain in-band production over the entire pulse, which leads to a sharp decrease in in-band power midway through the laser pulse. For high-mass sheets, it is possible to increase in-band production by simply increasing laser energy with minimal impact on CE. A stronger reduction in CE with increasing laser energy is identified for low-mass sheets, which limits the range of laser energies that can be employed for generating high in-band energies from this irradiation scheme. The identification of target conditioning schemes that maximize the mass in the sheet is, thus, key for improving both in-band production and CE from CO_2 laser-driven plasma sources.

The authors would like to thank Oscar Versolato, Wim van der Zande, Michael Purvis, Haining Wang, Elio Champenois, and Adam Higginson for useful discussions. We recognize prior unpublished work done at ARCNL by Yahia Mostafa on the topic of mass use in 2 μm laser-produced plasma. This work has been carried out at the Advanced Research Center for Nanolithography (ARCNL). ARCNL is a public–private partnership with founding partners UvA, VU, NWO-I, and ASML, and associate partner RUG. This work made use of the Dutch national e-infrastructure with the support of the SURF Cooperative using Grant No. EINF-5194.

AUTHOR DECLARATIONS

Conflict of Interest

The authors have no conflicts to disclose.

Author Contributions

Jorge Gonzalez: Conceptualization (equal); Data curation (equal); Formal analysis (equal); Investigation (equal); Visualization (equal); Writing – original draft (equal). **John Sheil:** Project administration (equal); Writing – review & editing (equal).

DATA AVAILABILITY

The data that support the findings of this study are available from the corresponding author upon reasonable request.

REFERENCES

[1]S. K. Moore, IEEE Spectrum **55**, 46 (2018).
[2]I. Fomenkov, D. Brandt, A. Ershov, A. Schafgans, Y. Tao, G. Vaschenko, S. Rokitski, M. Kats, M. Vargas, M. Purvis *et al.*, Adv. Opt. Technol. **6**, 173 (2017).
[3]O. O. Versolato, Plasma Sources Sci. Technol. **28**, 083001 (2019).
[4]G. O'Sullivan, B. Li, R. D'Arcy, P. Dunne, P. Hayden, D. Kilbane, T. McCormack, H. Ohashi, F. O'Reilly, P. Sheridan, E. Sokell, C. Suzuki, and T. Higashiguchi, J. Phys. B **48**, 144025 (2015).
[5]F. Torretti, J. Sheil, R. Schupp, M. M. Basko, M. Bayraktar, R. Meijer, S. Witte, W. Ubachs, R. Hoekstra, O. O. Versolato *et al.*, Nat. Commun. **11**, 2334 (2020).
[6]J. Sheil, O. O. Versolato, A. J. Neukirch, and J. Colgan, J. Phys. B **54**, 035002 (2021).
[7]A. Sasaki, A. Sunahara, H. Furukawa, K. Nishihara, S. Fujioka, T. Nishikawa, F. Koike, H. Ohashi, and H. Tanuma, J. Appl. Phys. **107**, 113303 (2010).
[8]F. Torretti, F. Liu, M. Bayraktar, J. Scheers, Z. Bouza, W. Ubachs, R. Hoekstra, and O. Versolato, J. Phys. D **53**, 055204 (2019).
[9]S. Bajt, J. B. Alameda, T. W. Barbee, Jr., W. M. Clift, J. A. Folta, B. B. Kaufmann, and E. A. Spiller, Opt. Eng. **41**, 1797 (2002).
[10]D. Kurilovich, A. L. Klein, F. Torretti, A. Lassise, R. Hoekstra, W. Ubachs, H. Gelderblom, and O. O. Versolato, Phys. Rev. Appl. **6**, 014018 (2016).
[11]D. Kurilovich, M. M. Basko, D. A. Kim, F. Torretti, R. Schupp, J. C. Visschers, J. Scheers, R. Hoekstra, W. Ubachs, and O. O. Versolato, Phys. Plasmas **25**, 012709 (2018).
[12]S. Yu. Grigoryev, B. V. Lakatosh, M. S. Krivokorytov, V. V. Zhakhovsky, S. A. Dyachkov, D. K. Ilnitsky, K. P. Migdal, N. A. Inogamov, A. Yu. Vinokhodov, V. O. Kompanets, Yu. V. Sidelnikov, V. M. Krivtsun, K. N. Koshelev, and V. V. Medvedev, Phys. Rev. Appl. **10**, 064009 (2018).
[13]R. A. Meijer, D. Kurilovich, K. S. E. Eikema, O. O. Versolato, and S. Witte, J. Appl. Phys. **131**, 105905 (2022).
[14]J. Hernandez-Rueda, B. Liu, D. J. Hemminga, Y. Mostafa, R. A. Meijer, D. Kurilovich, M. Basko, H. Gelderblom, J. Sheil, and O. O. Versolato, Phys. Rev. Res. **4**, 013142 (2022).
[15]S. Fujioka, M. Shimomura, Y. Shimada, S. Maeda, H. Sakaguchi, Y. Nakai, T. Aota, H. Nishimura, N. Ozaki, A. Sunahara, K. Nishihara, N. Miyanaga, Y. Izawa, and K. Mima, Appl. Phys. Lett. **92**, 241502 (2008).
[16]K. Nishihara, A. Sunahara, A. Sasaki, M. Nunami, H. Tanuma, S. Fujioka, Y. Shimada, K. Fujima, H. Furukawa, T. Kato, F. Koike, R. More, M. Murakami, T. Nishikawa, V. Zhakhovskii, K. Gamata, A. Takata, H. Ueda, H. Nishimura, Y. Izawa, N. Miyanaga, and K. Mima, Phys. Plasmas **15**, 056708 (2008).
[17]B. Liu, D. Kurilovich, H. Gelderblom, and O. O. Versolato, Phys. Rev. Appl. **13**, 024035 (2020).
[18]B. Liu, R. A. Meijer, J. Hernandez-Rueda, D. Kurilovich, Z. Mazzotta, S. Witte, and O. O. Versolato, J. Appl. Phys. **129**, 053302 (2021).
[19]B. Liu, R. A. Meijer, W. Li, J. Hernandez-Rueda, H. Gelderblom, and O. O. Versolato, Phys. Rev. Appl. **20**, 014048 (2023).
[20]A. Sunahara, A. Hassanein, K. Tomita, S. Namba, and T. Higashiguchi, Opt. Express **31**, 31780 (2023).
[21]K. Tomita, Y. Sato, S. Tsukiyama, T. Eguchi, K. Uchino, K. Kouge, H. Tomuro, T. Yanagida, Y. Wada, M. Kunushima, G. Soumagne, T. Kodama, H. Mizoguchi, A. Sunahara, and K. Nishihara, Sci. Rep. **7**, 12328 (2017).
[22]K. Tomita, Y. Pan, A. Sunahara, K. Kouge, H. Mizoguchi, and K. Nishihara, Sci. Rep. **13**, 1825 (2023).
[23]M. M. Basko, Phys. Plasmas **23**, 083114 (2016).
[24]M. M. Basko, J. Maruhn, and A. Tauschwitz, GSI Rep. **1**, 410 (2010).
[25]M. M. Basko, P. V. Sasorov, M. Murakami, V. G. Novikov, and A. S. Grushin, Plasma Phys. Controlled Fusion **54**, 055003 (2012).
[26]An. Tauschwitz, M. Basko, A. Frank, V. Novikov, A. Grushin, A. Blazevic, M. Roth, and J. A. Maruhn, High Energy Density Phys. **9**, 158 (2013).

[27]M. M. Basko, V. G. Novikov, and A. S. Grushin, Phys. Plasmas **22**, 053111 (2015).
[28]D. J. Hemminga, L. Poirier, M. M. Basko, R. Hoekstra, W. Ubachs, O. O. Versolato, and J. Sheil, Plasma Sources Sci. Technol. **30**, 105006 (2021).
[29]D. J. Hemminga, O. O. Versolato, and J. Sheil, Phys. Plasmas **30**, 033301 (2023).
[30]A. F. Nikiforov, V. G. Novikov, and V. B. Uvarov, *Quantum-Statistical Models of Hot Dense Matter: Methods for Computation Opacity and Equation of State* (Springer Science & Business Media, 2005), Vol. 37.
[31]I. Yu. Vichev, A. D. Solomyannaya, A. S. Grushin, and D. A. Kim, High Energy Density Phys. **33**, 100713 (2019).
[32]S. Faik, A. Tauschwitz, and I. Iosilevskiy, Comp. Phys. Commun. **227**, 117 (2018).
[33]R. M. More, K. H. Warren, D. A. Young, and G. B. Zimmerman, Phys. Fluids **31**, 3059 (1988).
[34]A. J. Kemp and J. Meyer-ter-Vehn, Nucl. Instrum. Methods Phys. Res., Sect. A **415**, 674 (1998).
[35]M. M. Basko and I. P. Tsygvintsev, Comput. Phys. Commun. **214**, 59–70 (2017).
[36]W. D. Kimura, Opt. Laser Technol. **88**, 263 (2017).
[37]B. V. Lakatosh, D. B. Abramenko, V. V. Ivanov, V. V. Medvedev, V. M. Krivtsun, K. N. Koshelev, and A. M. Yakunin, Laser Phys. Lett. **15**, 016003 (2017).
[38]J. Tang, D. Zuo, T. Wu, and Z. Cheng, Opt. Commun. **289**, 114 (2013).
[39]J. A. McKay, R. D. Bleach, D. J. Nagel, J. T. Schriempf, R. B. Hall, C. R. Pond, and S. K. Manlief, J. Appl. Phys. **50**, 3231 (1979).
[40]J. Sheil, O. Versolato, V. Bakshi, and H. Scott, Atoms **11**, 130 (2023).